PNAS RESEARCH ARTICLE | CHEMISTRY

Optimizing oxygen vacancies through grain boundary engineering to enhance electrocatalytic nitrogen reduction

Xiu Zhong[a,1], Enxian Yuan[b,1], Fu Yang[a,2], Yang Liu[a], Hao Lu[a], Jun Yang[c], Fei Gao[a], Yu Zhou[d], Jianming Pan[e], Jiawei Zhu[f], Chao Yu[a], Chengzhang Zhu[g], Aihua Yuan[a,2], and Edison Huixiang Ang[h,2]

Edited by Alexis Bell, University of California, Berkeley, CA; received April 24, 2023; accepted August 9, 2023

Electrocatalytic nitrogen reduction is a challenging process that requires achieving high ammonia yield rate and reasonable faradaic efficiency. To address this issue, this study developed a catalyst by in situ anchoring interfacial intergrown ultrafine MoO_2 nanograins on N-doped carbon fibers. By optimizing the thermal treatment conditions, an abundant number of grain boundaries were generated between MoO_2 nanograins, which led to an increased fraction of oxygen vacancies. This, in turn, improved the transfer of electrons, resulting in the creation of highly active reactive sites and efficient nitrogen trapping. The resulting optimal catalyst, MoO_2/C_{700}, outperformed commercial MoO_2 and state-of-the-art N_2 reduction catalysts, with NH_3 yield and Faradic efficiency of 173.7 μg h^{-1} mg^{-1}_{cat} and 27.6%, respectively, under − 0.7 V vs. RHE in 1 M KOH electrolyte. In situ X-ray photoelectron spectroscopy characterization and density functional theory calculation validated the electronic structure effect and advantage of N_2 adsorption over oxygen vacancy, revealing the dominant interplay of N_2 and oxygen vacancy and generating electronic transfer between nitrogen and Mo(IV). The study also unveiled the origin of improved activity by correlating with the interfacial effect, demonstrating the big potential for practical N_2 reduction applications as the obtained optimal catalyst exhibited appreciable catalytic stability during 60 h of continuous electrolysis. This work demonstrates the feasibility of enhancing electrocatalytic nitrogen reduction by engineering grain boundaries to promote oxygen vacancies, offering a promising avenue for efficient and sustainable ammonia production.

grain boundaries | oxygen vacancy | ammonia synthesis | nitrogen reduction | electrocatalyst

The process of converting N_2 to NH_3 is a widely employed industrial procedure for manufacturing fertilizers, chemicals, and pharmaceuticals (1, 2). Furthermore, this process is considered an eco-friendly approach, making it a valuable resource for sustainable energy use in the future (3–8). Currently, there are several approaches for synthesizing ammonia, including industrial ammonia synthesis, photocatalysis, biological enzyme nitrogen fixation, and electrocatalytic ammonia synthesis. Notably, the Haber–Bosch method is the main method used in industrial ammonia synthesis (1, 9–12), which operates at high temperatures (350 to 550 °C) and high pressures (150 to 350 atm), entails high energy usage, intricate equipment, and leads to significant carbon dioxide emissions and has a negative impact on the environment (13–17).

In contrast, the electrocatalytic nitrogen reduction reaction (NRR) occurs under ambient conditions, significantly reducing carbon dioxide emissions and environmental pollution (18–23). However, this approach faces challenges in practical implementation due to the low yield of ammonia and Faradaic efficiency (FE) resulting from weak adsorption interaction of N_2 molecules with the catalyst, high binding energy of N≡N bonds (24–26), and the competition with the hydrogen evolution reaction (HER) during the NRR process (27, 28). Building on the aforementioned information, numerous studies have explored the use of catalysts such as noble metals (29–31), transition metal [oxides, sulfides, nitrides, carbides (32–38)], and nonmetals (39, 40) to enhance nitrogen adsorption and reduce reaction barriers in NRR (41, 42). However, nonmetallic catalysts are typically characterized by weak electrical conductivity and high HER, while noble metal catalysts are restricted in their large-scale application due to their exorbitant cost and limited availability. Transition metals have abundant empty d-orbitals that can accept and donate electrons to N_2, thus promoting N_2 adsorption and activation, and improving NRR performance (43). Among these, Mo-based catalysts show great promise in electrocatalytic NRR due to their high inherent activity. For instance, Fei et al. have controlled the sulfur vacancies of MoS_2 by doping P for NRR research, resulting in a yield of NH_3 of 60.27 μg h^{-1} mg^{-1}_{cat} with an FE of 12.2% (44). Sun et al. have synthesized Mo_2N nanorods with high ammonia yield of 78.4 μg h^{-1} mg^{-1}_{cat} (45).

Significance

Ammonia (NH_3) production is vital for industrial and agricultural sectors, but the current Harper–Bosch process has negative environmental impacts. This study proposes an eco-friendly alternative through electrochemical nitrogen (N_2) reduction. However, challenges like slow kinetics, low N_2 solubility, and competition from hydrogen evolution reaction (HER) must be overcome. To address these, researchers developed a unique catalyst with ultrafine MoO_2 nanograins anchored on N-doped carbon fibers and optimized grain boundaries through thermal treatment. The resulting catalyst exhibited a high fraction of oxygen vacancies, enhancing reactive sites for efficient nitrogen trapping and NH_3 yield. This research holds great potential for environmentally sustainable ammonia production, offering far-reaching implications.

Author contributions: F.Y. designed research; X.Z. performed research; X.Z., E.Y., F.Y., Y.L., H.L., J.Y., F.G., Y.Z., J.P., J.Z., C.Y., C.Z., A.Y., and E.H.A. analyzed data; E.Y. performed the computational simulation; F.Y. supervision, funding acquisition and edited the paper; E.H.A. edited the paper; and X.Z., F.Y., and E.H.A. wrote the paper.

The authors declare no competing interest.

This article is a PNAS Direct Submission.

[1]X.Z. and E.Y. contributed equally to this work.

[2]To whom correspondence may be addressed. Email: fuyang@just.edu.cn, aihua.yuan@just.edu.cn, or edison.ang@nie.edu.sg.

This article contains supporting information online at https://www.pnas.org/lookup/suppl/doi:10.1073/pnas.2306673120/-/DCSupplemental.

Published September 25, 2023.

To enhance the surface catalytic activity of metal catalysts for NRR, researchers often tailor their size to improve the exposure of catalytic sites. The concept of atomically dispersed catalysts has been introduced to maximize atomic exposure and enhance surface energy. However, this approach may inadvertently hinder the trapping effect of N_2 molecules due to their weak adsorption on catalytic sites, which typically limits successive activation. Specifically, the surface adsorption of N_2 molecules on catalytic sites plays a crucial role in achieving a well-balanced interaction according to the Sabatier principle. To tackle this challenge, scientists have endeavored to customize the size of Mo-based oxides in order to achieve a favorable equilibrium between surface activity and trapping capability. Specifically, by tailoring these active metal oxides, more oxygen vacancies can be created, serving as effective trapping sites for capturing N_2 molecules during the electrocatalytic NRR process. It is important to note that N_2 molecules trapped by oxygen vacancies facilitate a more favorable metal-N_2 interaction, underscoring the crucial role of oxygen vacancies in the NRR process. However, optimizing the catalytic performance through the customization of active substances often comes at the expense of catalytic stability due to the high surface energy involved. Additionally, transition metal oxide catalysts generally exhibit poor conductivity, further complicating the attainment of high NRR activity (46). Enhancing the electron transfer transport is essential in order to facilitate the incorporation of highly active metallic species, thereby improving the electron transferring capacity and augmenting the reactivity.

In this study, we developed a universal technique to integrate densely distributed MoO_2 with interfacial intergrown ultrafine MoO_2 nanograins into carbon nanofibers. The carbon fiber could accommodate these active metal oxides and further act as the electron transporting carrier during the electrocatalytic NRR process. The interfacial characteristics of MoO_2 nanograins have the potential to generate a greater number of active interfacial reactive sites and defect structures, such as oxygen vacancies. This configuration proves advantageous for both the trapping and activation of N_2 molecules. Furthermore, by constructing such a configuration, the resulting ultrafine MoO_2 nanograins can achieve stability through intermetallic interplay and metal–support interaction, all while maintaining their activity. In the work, by optimizing the oxygen vacancies of intergrown MoO_2 nanograins through thermal treatment, the MoO_2/C_{700} catalyst exhibited a record-high NRR performance in all reported transition metal-based catalysts and the second-highest performance overall, including noble metal-based catalysts. The catalyst had an NH_3 yield of 173.7 μg h^{-1} mg^{-1}_{cat} and an FE of 27.6% when the potential was −0.7 V vs. RHE in 1 M KOH electrolyte, and it maintained good stability after 60 h of continuous electrolysis. This study provides a simple and effective method for designing high-performance NRR electrocatalysts with high activity and stability.

Results and Discussion

The diagram in Fig. 1*A* depicts the synthetic representation of the MoO_2/C_x catalyst series obtained through electrospinning (where x represents the calcination temperature). The MoO_2/C precursor before calcination was examined using scanning electron microscopy (SEM), revealing nanofibers with a diameter of approximately 100 nm (shown in *SI Appendix*, Fig. S1 *A* and *B*). Fig. 1 *B*–*E* demonstrates that the catalysts calcined at temperatures ranging from 600 °C to 900 °C maintained their nanofiber-like morphology. The metal concentration extracted from the Inductively Coupled Plasma (ICP) measurement of Mo in the MoO_2/C_x catalysts (*SI Appendix*, Table S1) increased gradually with an increase in treatment temperature. This is attributed to the loss of carbon composition in the fiber due to higher carbonization temperatures. TEM technique was used to identify the microscale structure of MoO_2/C_x, revealing uniform dispersion of Mo element into the carbon fiber and scattered MoO_2 nanocrystals with low crystallinity on the carbon fiber for MoO_2/C_{600} (as shown in *SI Appendix*, Fig. S2). The presence of darker regions observed on the carbon fiber surface in the TEM image (Fig. 1*F*) of MoO_2/C_{700} could be attributed to the formation of MoO_2 nanoparticles that are adhered to the surface. HRTEM and FFT images of MoO_2/C_{700} at a specific position (as shown in Fig. 1 *G* and *H*) reveal abundant diversified adjacent crystalline facets with different interplanar spacings, corresponding to different crystal planes of MoO_2 nanocrystals, indicating the existence of abundant grain boundaries. The average size of each grain in the selected region is approximately 6.8 nm. With an increase in carbonization temperature, agglomeration of MoO_2 particles on the surface of carbon fiber was observed for MoO_2/C_{800} and MoO_2/C_{900} (as shown in *SI Appendix*, Figs. S3*A* and S4*A*). High Resolution Transmission Electron Microscopy (HRTEM) and Fast Fourier Transform (FFT) images of MoO_2/C_{800} and MoO_2/C_{900} at specific locations (as shown in *SI Appendix*, Figs. S3 *B* and *C* and S4 *B* and *C*) demonstrate lattice stripe belonging to MoO_2. The interfacial behavior of nanocrystals in MoO_2/C_{800} and MoO_2/C_{900} was lesser compared to MoO_2/C_{700}. The abundant interfacial engineering observed in MoO_2/C_{700}, primarily attributed to the distinct crystal faces present in adjacent grains, plays a crucial role in influencing the active state of interfacial catalytic sites during the electrocatalytic nitrogen reduction to ammonia process. The formed nanograins cause a positive relationship between oxygen vacancy sites and interfacial behavior, which is beneficial to obtain more trapping sites for capturing N_2 molecules. Elemental mapping analysis (as shown in Fig. 1*I* and *SI Appendix*, Figs. S2*D*, S3*D*, and S4*D*) revealed the dominant elemental composition and uniform distribution of C, Mo, N, and O over the carbon fiber catalyst.

To comprehend the structural model and elemental coordination state of the catalyst, various analytical techniques were employed on MoO_2/C_x, including the acquisition and identification of XRD (X-ray diffraction) patterns, Raman spectra, and XPS (X-ray photoelectron spectroscopy) spectra, as shown in Fig. 2. As displayed in Fig. 2*A*, MoO_2/C_{600} exhibits a broad diffraction at 20 to 30, indicating the prevalence of an amorphous structure of carbon fiber. The lack of diffraction of crystalline molybdenum oxides suggests that molybdenum oxides in MoO_2/C_{600} may be in an amorphous state. On the other hand, the presence of a crystalline diffraction peak that corresponds to the cubic phase MoO_2 (PDF#32-0671) in MoO_2/C_{700}, MoO_2/C_{800}, and MoO_2/C_{900} denotes the high-temperature induced polycrystalline structure of MoO_2 in carbon fiber. The diffraction curves of MoO_2/C_{800} and MoO_2/C_{900} exhibit the diffraction behavior of metallic Mo, in addition to the diffraction of MoO_2. The presence of metallic Mo in the catalyst may have resulted from the reduction of MoO_2 during high-temperature treatment in an inert nitrogen atmosphere, which could lead to a competitive HER reaction. The grain size of MoO_2 in MoO_2/C_{700}, MoO_2/C_{800}, and MoO_2/C_{900} was calculated using the Scherrer Formula. The calculated average particle size of MoO_2/C_{700} is 6.4 nm, which is consistent with the statistical results of the HRTEM image (Fig. 1*G*). The calculated grain sizes of MoO_2/C_{800} and MoO_2/C_{900} are 8.5 nm and 25.6 nm, respectively, indicating that the higher calcination temperature induced the agglomeration and growth of MoO_2 nanograins, which subsequently reduces the interfacial behavior and defects of metal species. Moreover, the small size of MoO_2 nanograins in the MoO_2/C_{700} catalyst could lead to sufficient exposure of surface-active centers. In this study, to demonstrate the superior

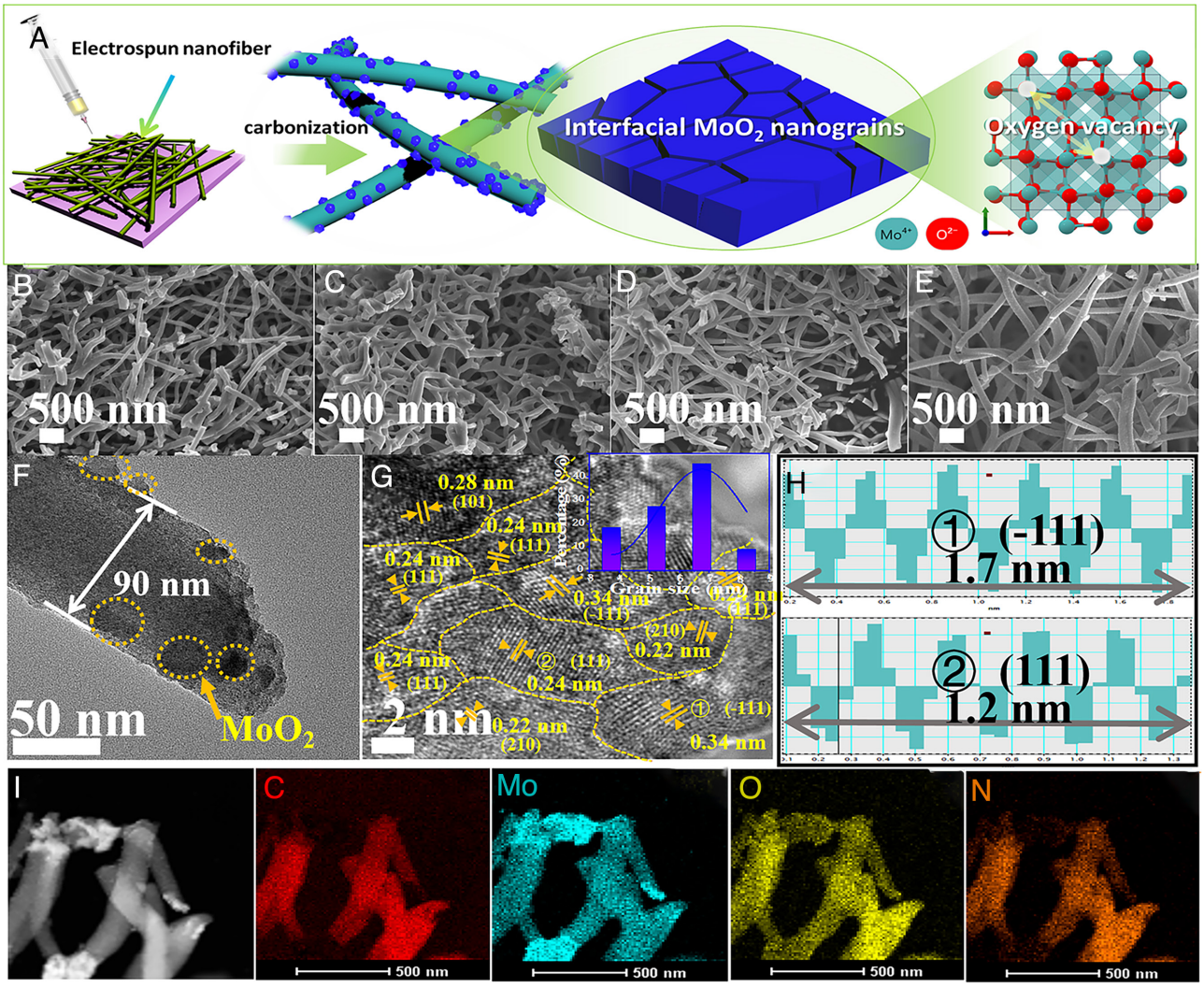

Fig. 1. (*A*) Schematic representation of the synthesis of MoO_2/C_x. Representative SEM images of catalyst MoO_2/C_x: (*B*) MoO_2/C_{600}, (*C*) MoO_2/C_{700}, (*D*) MoO_2/C_{800}, (*E*) MoO_2/C_{900}, (*F*) TEM image, (*G*) high-resolution TEM image with insert grain size distribution and (*H*) its corresponding specific FFT results, (*I*) as well as the element mapping images of representative catalyst MoO_2/C_{700}.

NRR activity of the catalyst MoO_2/C_{700} for electrospinning synthesis, a comparative catalyst, MoO_2-C_{700}, was synthesized by mechanical mixing. The XRD diffraction pattern showed that MoO_2/C_{700} was successfully synthesized (as shown in *SI Appendix*, Fig. S5). Furthermore, the Raman spectra of MoO_2/C_x and pure carbon fiber were analyzed to identify the structure of the carbon framework of carbon fiber (as shown in Fig. 2*B*). The I_D/I_G peak intensity ratio generally decreased with increasing calcination temperature, indicating a lower defect level that could benefit electron transfer over the carbon fiber. However, the enlarged particle size of active metal species might compromise the reactivity of MoO_2. To determine the valence state change and coordination environment of the catalyst MoO_2/C_x, XPS characterization and corresponding analysis were conducted. The survey of XPS (*SI Appendix*, Fig. S6) revealed that the four temperature-calcined catalysts all contained C, N, O, and Mo elements. The energy level spectra of C 1s, O 1s, and Mo 3d of the MoO_2/C_x series were analyzed in detail and presented in Fig. 2 *D*–*F*. The XPS characterization and corresponding analysis were utilized to determine the valence state change and coordination environment of the MoO_2/C_x catalyst. The C 1s spectra of the different catalysts are shown in Fig. 2*D* and exhibit two types of core level peaks at binding energies of 284.6 eV and 286.2 eV, corresponding to C-C and C-O-Mo bonds, respectively. It is noteworthy that the MoO_2/C_{700} catalyst shows the largest fraction of C-O-Mo species, indicating stronger metal–carbon support interaction. This interaction facilitates electron transfer and enhances the stability of active metals during the electrocatalytic process. Specifically, the adsorption of N_2 molecules on the MoO_2/C_{700} catalyst can receive more electrons donated to the antibonding orbital of the N≡N bond. Moreover, the Mo 3d orbital contains an unoccupied empty. In Fig. 2*E*, the O 1s spectra of the four catalysts exhibit three energy level peaks with binding energies of 530.4 eV, 531.4 eV, and 532.6 eV, corresponding to lattice oxygen (O_L), adsorbed oxygen (O_A) from oxygen vacancies (O_V), and C-O-M species. The presence of oxygen vacancies was further confirmed by electron spin resonance (ESR) with the highest signal intensity observed in the MoO_2/C_{700} catalyst (Fig. 2*C* and *SI Appendix*, Fig. S7). The XPS results show that the MoO_2/C_{700} catalyst has the highest fraction of oxygen vacancies, which is advantageous for N_2 adsorption over the O_V and NRR performance. However, an excess of lattice oxygen can favor the HER. Therefore, regulating the fraction of oxygen vacancy and lattice oxygen could enhance the NRR process while limiting the competitive reaction. Additionally, the formation of C-O-M species facilitates the electron transfer between the metal species and support during the electrocatalytic process. Fig. 2*F*

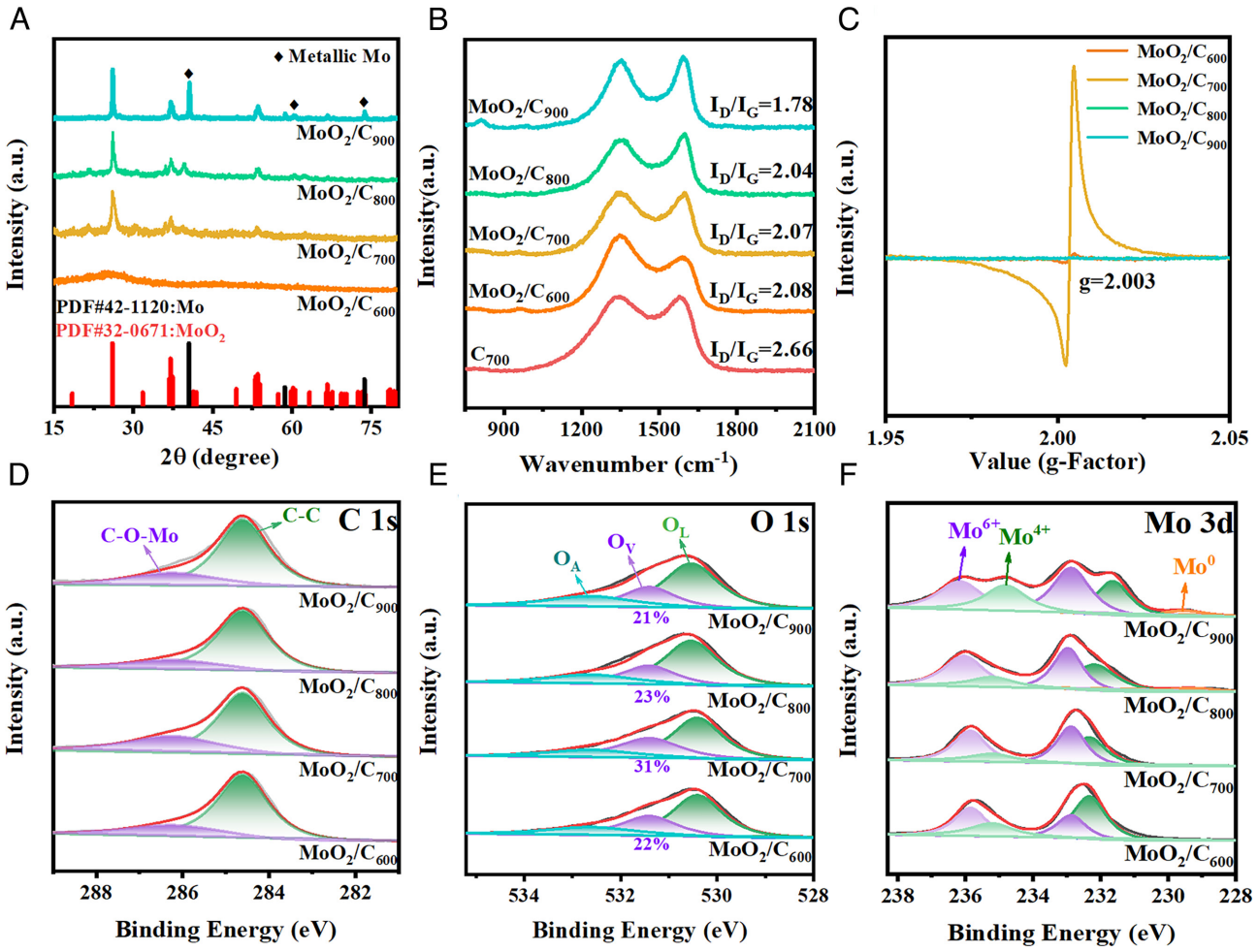

Fig. 2. (*A*) XRD patterns; (*B*) Raman spectra; (*C*) ESR spectra; XPS spectra: (*D*) C 1s; (*E*) O 1s; (*F*) Mo 3d core level spectra of catalysts MoO_2/C_x.

illustrates the Mo 3d spectra of the four comparative catalysts, which exhibit two types of Mo, including Mo^{4+} and Mo^{6+} species with binding energies of 232.3 eV and 235.2 eV, and 232.9 eV and 235.9 eV, respectively. At calcination temperatures of 800 C and 900 C, the catalyst produces metallic elemental Mo, as demonstrated by the appearance of Mo^0 at binding energies of 229.3 eV and 234.3 eV. The specific content of Mo species was collected (as shown in *SI Appendix*, Table S2). It should be noted that the Mo^0 present in the Mo3d is faint, which could be due to the surface oxidation behavior of Mo particles. Furthermore, the presence of metallic elemental Mo causes the shift of Mo^{4+} and Mo^{6+} due to the interaction between the species. It is our belief that the production of metallic Mo species in the catalyst can negatively affect the NRR performance due to their competitive HER activity. The comparative catalysts exhibit nitrogen adsorption and desorption capacity (*SI Appendix*, Fig. S8*A* and Table S3) that is comparable to that of pure carbon (C_{700}) (22.5 $cm^3\ g^{-1}$), and the pore size distribution derived from the adsorption curves of different samples (*SI Appendix*, Fig. S8*B*) is predominantly concentrated in the micropore area (1 to 2 nm), which is advantageous for capturing low-concentration N_2 molecules.

The NRR performance of the MoO_2/C_x catalyst series was evaluated using a standard three-electrode system in an H-type cell under ambient conditions. The potential window range below −0.4 V vs. RHE exhibited a clear difference (as shown in Fig. 3*A* and *SI Appendix*, Fig. S9 *A*–*C*). The LSV (Linear scanning voltammetry) polarization curves of the catalyst MoO_2/C_x in N_2-saturated electrolyte showed a significantly higher current density than in Ar-saturated electrolyte, implying that all the MoO_2/C_x catalysts possess potential NRR catalytic activity in 1 M KOH electrolyte. In addition, Fig. 3*B* illustrated that the current density of the catalyst in N_2-saturated electrolyte displays a trend of volcanic type with increasing calcination temperature, with MoO_2/C_{700} exhibiting the highest current density among all the counterparts. This finding indicates that MoO_2/C_{700} possesses the best NRR performance. Furthermore, to assess the catalyst MoO_2/C_x performance, the catalyst ink supported on carbon cloth was used as the working electrode with N_2 bubbling at a rate of 20 mL min^{-1} for 2 h of chronoamperometric electrolysis test. Stable current–time curves at different potentials indicated great activity stability of used catalysts (as shown in Fig. 3*C* and *SI Appendix*, Figs. S11*A*, S12*A*, and S13*A*). The absorbance curves of the electrolyte in the cathode compartment after electrolysis at different potentials (see shown in Fig. 3*D* and *SI Appendix*, Figs. S11*B*, S12*B*, and S13*B*). The average ammonia yield and FE of catalyst MoO_2/C_x after 2 h at different potentials were determined according to the standard calibration curve of NH_3 (*SI Appendix*, Fig. S10), the accumulated charge of the electrolyte in the anode compartment, and the cathode compartment and the generated ammonia concentration (Fig. 4*E* and *SI Appendix*, Figs. S11*C*, S12*C*, and S13*C*).

The variation of the average ammonia yield of the catalyst MoO_2/C_{700} showed a volcanic type of change as the potential became more negative. The highest absorption intensity at 655 nm was achieved at −0.7 V vs. RHE, and the corresponding NH_3

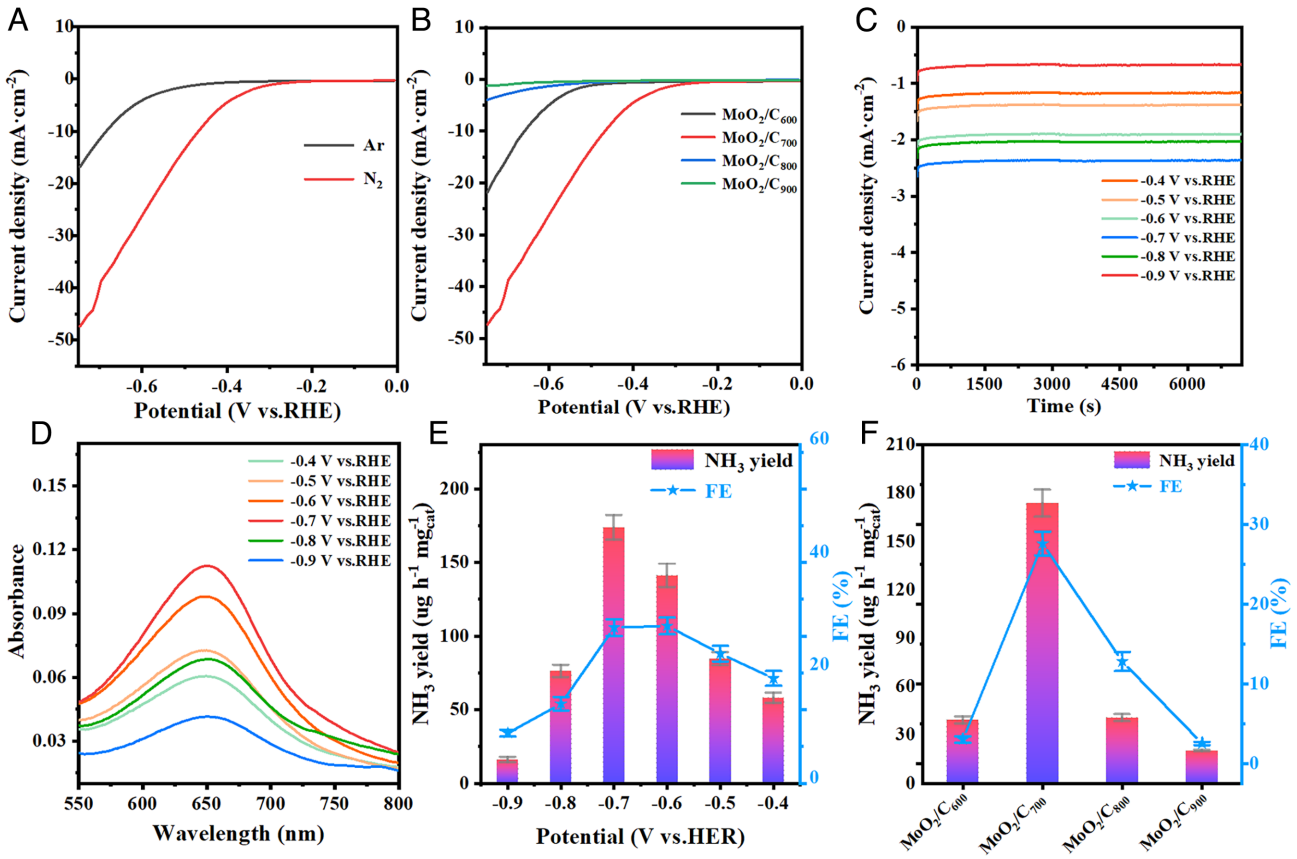

Fig. 3. (*A*) LSV curves of the catalyst MoO_2/C_{700} in 1 M KOH electrolyte saturated with N_2 and Ar; (*B*) LSV curve of the catalysts MoO_2/C_x in a 1 M KOH electrolyte saturated with N_2, respectively; (*C*) I-T curves of catalyst MoO_2/C_{700} in N_2; (*D*) UV-visible spectra of electrolyte in cathode chamber stained with indophenol indicator; (*E*) NH_3 yield and FE at different potentials; (*F*) comparison of electrocatalytic NRR activity of different catalysts.

yield was the highest, up to 173.7 μg h^{-1} mg^{-1}_{cat} (Fig. 3*E*). The FE also showed the same trend, with an FE of 27.6% at −0.7 V vs. RHE. The NH_3 yield and FE of the MoO_2/C_{700} catalyst were significantly reduced when the applied potential was lower than −0.7 V vs. RHE. This reduction was attributed to the enhanced HER competition reaction affecting the contact of N_2 molecules with the surface-active sites, and the HER dominated the electrocatalytic reaction at that point. Compared to other MoO_2/C_x counterparts at −0.7 V vs. RHE, it was found that the average ammonia yield and FE of MoO_2/C_{700} were the best (Fig. 3*F*). This was mainly due to the abundant interfacial behavior along with unique oxygen vacancy and beneficial metal-support interplay of MoO_2/C_{700}.

Extensive research has been conducted to investigate the source of nitrogen in the NRR reaction. To this end, a series of controlled experiments were performed based on prior research. When the electrocatalytic experiment was conducted with argon as the feed gas at −0.7 V vs. RHE, the UV-vis absorption peak intensity was comparable to that of the blank electrolyte, which was much lower than that with nitrogen as the feed gas (*SI Appendix*, Fig. S14). This indicates that NH_3 is not produced when argon is utilized as the feed gas. Similar results were obtained when nitrogen was used as the intake gas at open circuit voltage (*SI Appendix*, Fig. S14). The above findings demonstrate that the observed NH_3 was generated through the electrochemical reduction of N_2 and not from the contamination of the air or the catalyst itself. The generation of intermediate by-products and the complex reaction pathways in NRR have drawn attention to the possible formation of by-product N_2H_4, which was determined by the Watt and Crisp method, and the corresponding calibration curve (see shown in *SI Appendix*, Fig. S15). The absorbance curves of the electrolyte in the cathode chamber after electrolysis at various potentials were stained with an indicator for 15 min. No absorbance at 460 nm was detected, thus excluding the possibility of the by-product hydrazine (N_2H_4) in the electrochemical NRR process (as shown in Fig. 4*A* and *SI Appendix*, Fig. S16). Therefore, it can be inferred that the synthesized catalyst MoO_2/C_x demonstrates excellent selectivity for the electrocatalytic NRR reaction.

To investigate the improved NRR performance of MoO_2/C_{700}, various catalyst samples were subjected to electrochemical impedance spectroscopy (EIS) tests to analyze the charge transfer kinetics. As illustrated in Fig. 4*B*, the catalyst MoO_2/C_{700} exhibited a lower charge transfer resistance than the catalysts calcined at different temperatures, implying that charge transfer could have a significant impact on promoting the electrochemical NRR reaction. Carbon fiber provides excellent support for the integrated nanograins of MoO_2, facilitating charge transfer. The electrochemical surface area (ECSA) was determined by measuring the double-layer capacitance (C_{dl}) (*SI Appendix*, Fig. S17). MoO_2/C_{700} (12.71 mF cm^{-2}) exhibits a higher ECSA than MoO_2/C_{600} (1.02 mF cm^{-2}), indicating the presence of more active sites in MoO_2/C_{700}. However, MoO_2/C_{800} (23.27 mF cm^{-2}) and MoO_2/C_{900} (59.02 mF cm^{-2}) have higher ECSA than MoO_2/C_{700} (12.71 mF cm^{-2}), which may be due to higher metal loading in the catalyst (as shown in Fig. 4*C*). Nevertheless, the competition reactivity of hydrogen evolution is constantly enhanced with the emergence of elemental Mo, which eventually dominates the reaction, leading to the underutilization of exposed active sites of MoO_2/C_{800} and MoO_2/C_{900} for N_2 and a reduction in NRR activity. To assess the NRR performance of the MoO_2/C_{700} catalyst in

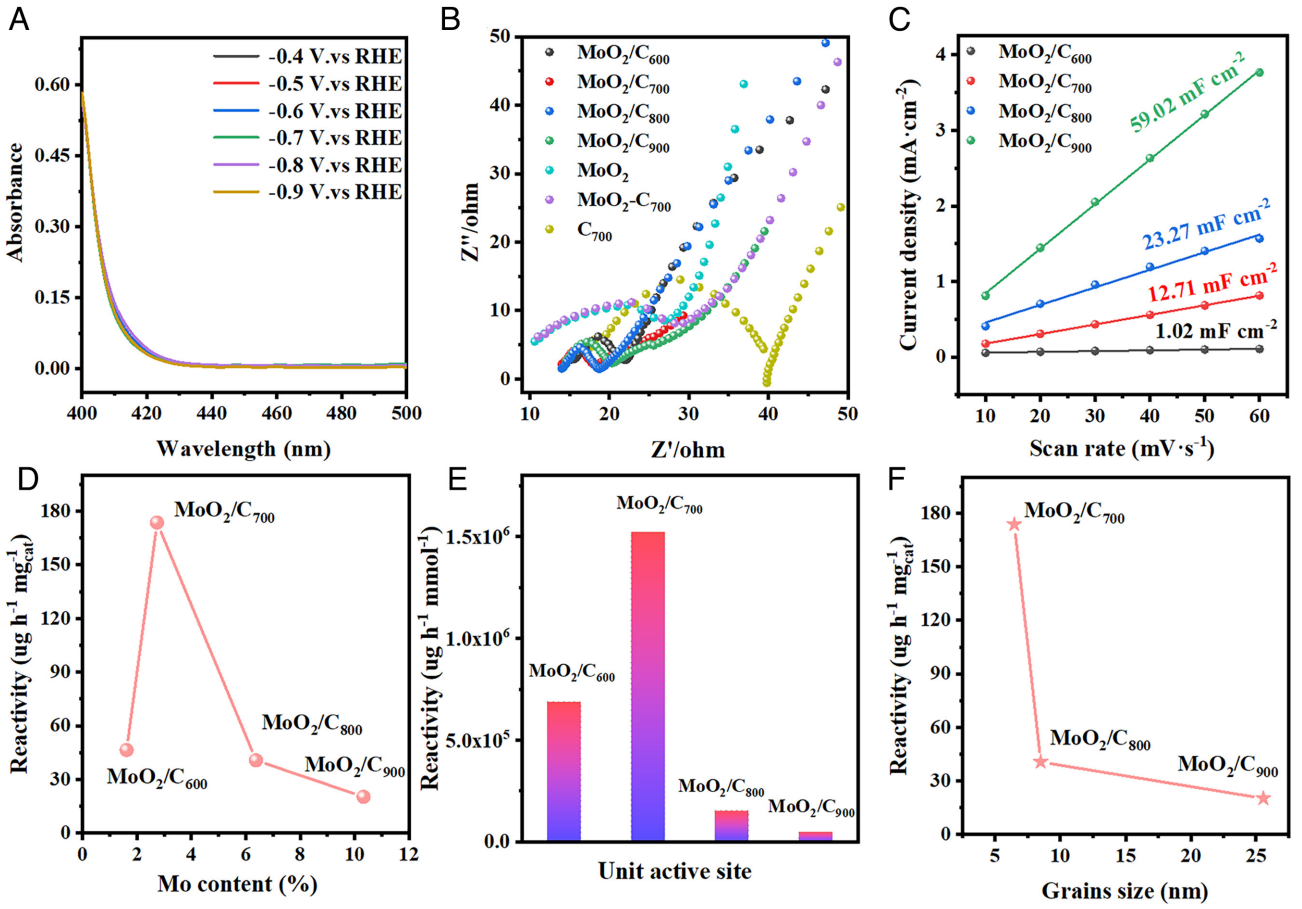

Fig. 4. (*A*) UV-visible spectra of electrolyte for MoO_2/C_{700} electrolysis at different potentials (watt and Chris method) after 2 h, (*B*) electrochemical impedance spectra (EIS) for different MoO_2/C_x samples, (*C*) charging current density difference and cyclic voltammetry (CV) scanning rate of catalyst MoO_2/C_x, (*D*) NH_3 yield of comparative catalysts MoO_2/C_x with measured Mo content at the potential of −0.7 V vs. RHE, (*E*) Mo content normalized NH_3 yield of the catalyst MoO_2/C_x at a potential of −0.7 V vs. RHE, and (*F*) NH_3 yield of catalyst MoO_2/C_x with measured grain size by Scherrer formula at the potential of −0.7 V vs. RHE.

comparison to MoO_2/C_{800} and MoO_2/C_{900} with higher Mo loading, Fig. 4*D* displays that MoO_2/C_{700} shows superior NRR activity, despite its modest Mo content. To further analyze the atom activity of Mo in NRR, the normalized NH_3 yield of MoO_2/C_x was measured based on the unit Mo sites. Fig. 4*E* illustrates the evolutive normalized NRR activity of different catalysts, which indicates that MoO_2/C_{700} continues to exhibit the most unit atom activity of Mo compared to other catalysts, emphasizing the outstanding NRR performance of MoO_2/C_{700}. Additionally, based on the ECSA results, it is suggested that a considerable number of Mo centers might be masked in the bigger aggregated particles of MoO_2/C_{800} and MoO_2/C_{900}. Moreover, due to the precipitation of metallic Mo in the MoO_2/C_{800} and MoO_2/C_{900} catalysts, the NRR performance is reduced, as observed through the corresponding NH_3 yield and FE. In comparison to MoO_2/C_{700}, the reduced NRR activity of MoO_2/C_{600} can be attributed to the inferior crystallinity and insufficient oxygen vacancy of Mo oxides resulting from the lower calcination temperature of the catalyst, which limits the number of active sites and trapping sites that can participate in the NRR process. To investigate the interfacial effect caused by grain size on catalytic activity, the electrocatalytic NRR performance of MoO_2/C_x samples with different active metal grain sizes obtained by XRD was compared. As shown in Fig. 4*F*, MoO_2/C_{700} exhibits the best NRR activity, including the highest NH_3 yield and FE, among the comparative catalysts. This can be ascribed to the smaller grain size and interfacial behavior leading to the larger exposed surface of active metal species and more abundant oxygen vacancies, which facilitate greater contact and trapping effect between the active site of the catalyst and N_2, thereby contributing to the higher NRR reactivity of the catalyst.

The durability of a catalyst is an essential aspect that affects its practical applications besides its NRR activity. Therefore, the stability of MoO_2/C_{700} was assessed by conducting continuous cycle tests and long-term chronoamperometric tests. In this regard, the electrolyte was replaced every 2 h, and four consecutive cycle tests were carried out at −0.7 V vs. RHE, without altering the electrode and Nafion 117 membrane. The results depicted in Fig. 5*A* showed that MoO_2/C_{700} exhibited no significant decline in NH_3 yield and FE, indicating that it possesses good electrocatalytic NRR stability under ambient conditions. Furthermore, the catalyst displayed no substantial variation in current density during continuous chronoamperometric measurements at −0.7 V vs. RHE for 60 h, as illustrated in Fig. 5*B*. This finding further emphasizes the high stability of MoO_2/C_{700} catalysts for electrocatalytic ammonia synthesis. To assess the extent of the NRR activity of the MoO_2/C_{700} catalyst, we conducted a comprehensive comparison of the NH_3 yield and FE of the catalyst with 60 other Mo-based electrocatalysts that have been recently reported. The radar diagram in Fig. 5*C* and *SI Appendix*, Table S4, illustrate the comparison results. As evidenced, the NH_3 yield value of MoO_2/C_{700} in our study sets an unique advantage among all other transition metal-based catalysts reported so far, while still demonstrating a considerable FE

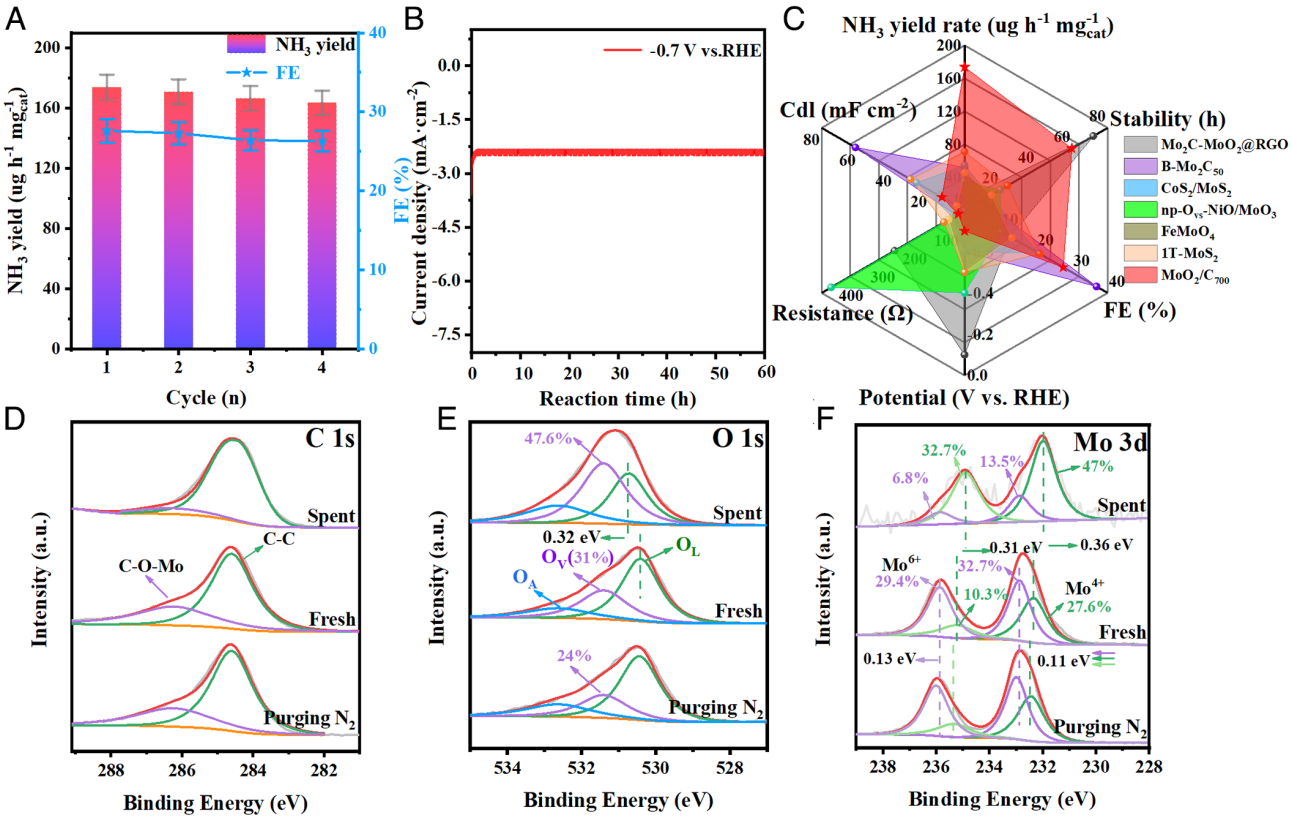

Fig. 5. (*A*) The NH_3 yield rate and FE of the catalyst MoO_2/C_{700} during four continuous NRR cycles at −0.7 V vs. RHE; (*B*) the charge current density test of continuous reaction over MoO_2/C_{700} for 60 h. (*C*) A multidimensional comparison of the NRR performance of the catalyst MoO_2/C_{700} with recently developed several typical molybdenum-based catalysts, XPS result comparison of fresh, spent MoO_2/C_{700} catalysts: (*D*) C 1s, (*E*) O 1s, (*F*) Mo 3d.

at such a high yield. To our knowledge, the obtained NH_3 yield value in this study outperforms most reported the-state-of-the-art catalysts (*SI Appendix*, Table S4, Entry 53). This finding further underscores the remarkable superiority of the catalyst and breakthrough in the realm of NRR.

XPS analysis was performed on the spent MoO_2/C_{700} catalyst to investigate the electron transfer that occurred on the surface-active sites during the reaction (as shown in Fig. 5 *D*–*F*). The intensity of C-O-Mo peak was reduced, indicating that the edge active Mo sites may have participated in the activation of N_2, causing the C-C peak to shift by 0.3 eV (Fig. 5*D*). Furthermore, the O 1s spectrum identified the lattice oxygen O_L responsible for N_2 activation, resulting in a 0.32 eV decrease and shift, resulting in an increase in the fraction of oxygen vacancies O_V (Fig. 5*E*). As the cathode compartment continued to accumulate charges during the reaction, Mo^{4+} and Mo^{6+} rearranged on the catalyst surface. To investigate the adsorption and activation of N_2 on the MoO_2/C_{700} catalyst, a simulation of the reaction environment was conducted, involving the catalyst and N_2 in the electrocatalytic NRR process. The MoO_2/C_{700} catalyst was subjected to in situ XPS analysis in a nitrogen atmosphere, and the results were compared with the XPS results of the catalyst before the reaction. As depicted in Fig. 5*D*, during in situ XPS, the C-O-Mo bond partakes in the activation of the N≡N bond, leading to an electron transfer between C-O-Mo and N≡N and a subsequent 0.1 eV shift in the signal peak. Furthermore, because O_V functions as the trapping site for nitrogen adsorption, some oxygen vacancies are consumed during the test, resulting in a 24% reduction in the fraction of oxygen vacancies of MoO_2/C_{700} evidenced by in-situ XPS (Fig. 5*E*). Finally, in the empty 3d orbital, Mo accepts the lone pair of electrons on N≡N, leading to a certain shift in both Mo^{4+} and Mo^{6+} in the in situ XPS of Mo (Fig. 5*F*). To confirm the benefits of smaller particle size and rich interfacial structure, as well as the strong C-O-Mo interaction and oxygen vacancies in the synthesized MoO_2/C_{700}, we compared its electrocatalytic NRR performance with that of several other catalysts, including pure carbon fiber C_{700}, mechanically mixed MoO_2-C_{700}, and commercialized MoO_2, all tested under the same conditions. The results revealed that the catalyst MoO_2-C_{700} had an ammonia synthesis rate of 1.52 μg h^{-1} mg^{-1}_{cat} and an FE of 0.08% at −0.7 V vs. RHE (*SI Appendix*, Fig. S18), while commercial MoO_2 displayed no NRR activity at −0.7 V vs. RHE and achieved the highest ammonia synthesis efficiency at −0.4 V vs. RHE, with an NH_3 yield of 10.4 μg h^{-1} mg^{-1}_{cat} and an FE of 4.8% (*SI Appendix*, Fig. S19). Our findings demonstrate that the NH_3 yield of the synthesized catalyst MoO_2/C_{700} is 114.3 times that of the mechanically mixed catalyst MoO_2-C_{700}, 16.7 times that of the commercialized MoO_2, and the FE is 345 times that of the mechanically mixed catalyst MoO_2-C_{700}, which is 5.8 times that of the commercialized MoO_2. In summary, the MoO_2/C_{700} catalyst we prepared exhibits comprehensive superiority in the NRR, thanks to the aforementioned advantages.

The trapping model of N_2 over O_V-free and O_V-rich MoO_2 during electrocatalytic nitrogen reduction is illustrated in Fig. 6*A*. The Figure indicates that the oxygen vacancy in MoO_2 has a strong ability to trap N_2, while O_V-free MoO_2 is susceptible to N_2 escaping from its surface. To investigate the mechanism behind the improved catalytic activity of MoO_2/C_{700} compared to O_V-free MoO_2 in the electrocatalytic synthesis of ammonia, density functional theory (DFT) calculations were conducted. The reaction

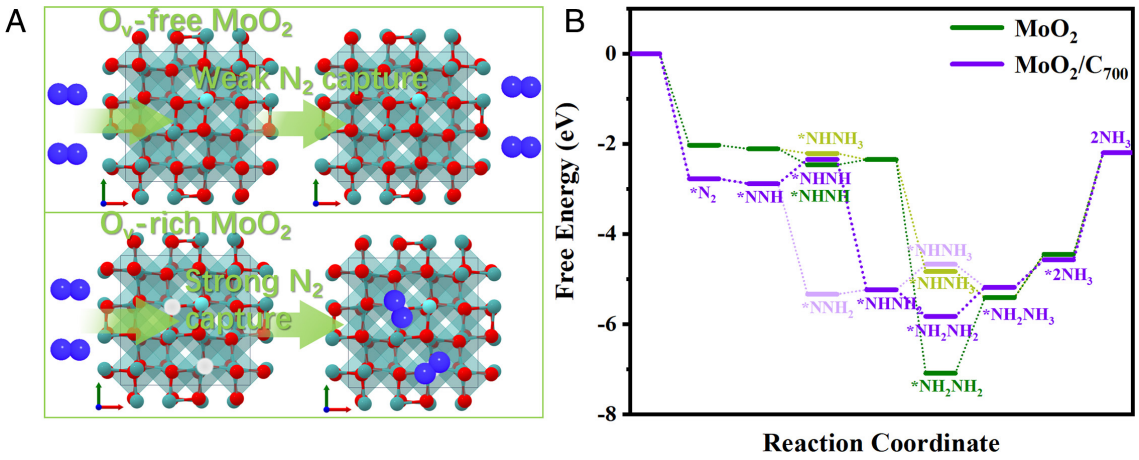

Fig. 6. (*A*) The description of nitrogen captured by oxygen vacancy of O_V-free and O_V-rich MoO_2 and (*B*) reaction pathways of NRR over oxygen vacancy–bearing MoO_2 in MoO_2/C_{700} nanocomposites and oxygen vacancy–free MoO_2 and the corresponding change of Gibbs free energy.

pathways of NRR over oxygen vacancy–bearing MoO_2 in MoO_2/C_{700} nanocomposites and oxygen vacancy–free MoO_2, as well as the corresponding change in Gibbs free energy, are depicted in Fig. 6*B*. During the process of electrocatalytic nitrogen reduction, N_2 molecules undergo reduction and protonation by electrons and protons. Initially, N_2 molecules are chemisorbed on the surface of MoO_2/C_{700} and pure MoO_2, with adsorption-free energies (ΔG^*_{N2}) of −2.78 eV and −2.03 eV, respectively. This confirms that oxygen vacancy–bearing MoO_2 synthesized through electrospinning and temperature control is favorable for N_2 adsorption. It is worth mentioning that most molybdenum-based catalysts face a large energy barrier for the first H to be added to NN. However, MoO_2/C_{700} exhibits a reduced ΔG^*_{NNH} (−2.89 eV) due to the presence of O_V in MoO_2, which significantly reduces the energy barrier and promotes the splitting of N≡N. The formation of NH_2NH_2 via the incorporation of a fourth H is known as the alternate pathway, which is energetically more favorable than the distal pathway with an energy barrier of −5.83 eV. Thus, the N_2 electrocatalysis on MoO_2/C_{700} tends to proceed through the alternate pathway. However, when the second NH_3 molecule is released, additional energy input is required to escape from the oxygen vacancy–bearing MoO_2 surface due to the strong interaction between the MoO_2 and NH_3. For oxygen vacancy–free MoO_2, although the energy barrier of ΔG_{NH2NH2} of the alternate path is lower than that of ΔG^*_{NHNH3} of the distal path, additional energy is required for the subsequent formation of $^*NH_2NH_3$. Therefore, the oxygen vacancy–free MoO_2 follows a distal mechanism in the electrocatalytic NRR process, which is consistent with most reported works. The reaction steps of NRR over vacancy-free MoO_2 and vacancy-bearing MoO_2 can be depicted as *SI Appendix*, Fig. S20. The catalytic activity enhancement mechanism of MoO_2/C_{700} compared to O_V-free MoO_2 for electrocatalytic synthesis of ammonia was further studied by DFT calculations, which are illustrated in Fig. 6*B*.

Conclusion

In summary, through fine-tuning the thermal treatment parameters, a significant amount of grain boundaries was induced among the MoO_2 nanograins, causing a higher portion of oxygen vacancies to emerge. As a consequence, electron transfer was enhanced, leading to the formation of exceedingly active catalytic sites that were effective in capturing nitrogen. The optimized MoO_2/C_{700} catalyst exhibited excellent NRR performance with NH_3 with a yield of 173.7 μg h^{-1} mg^{-1}_{cat} and an FE of 27.6% at −0.7 V vs. RHE in a 1 M KOH solution, which is currently the highest yield among all molybdenum-based catalysts used in the electrocatalytic NRR. Additionally, the catalyst demonstrated appreciable NRR stability over a 60 h reaction process. The preparation method of the catalyst MoO_2/C_{700} combines low cost, simplicity, and time-saving, making it particularly important for large-scale applications.

Data, Materials, and Software Availability. All study data are included in the article and/or *SI Appendix*.

ACKNOWLEDGMENTS. This work was financially supported by the National Natural Science Foundation of China (21908085), the Natural Science Foundation of Jiangsu Province, China (BK20190961), and the Postdoctoral Research Foundation of Jiangsu Province (2020Z291). The present study was also supported by the Jiangsu Provincial Key Laboratory of Environmental Science and Engineering (No. JSHJZDSYS-202103).

Author affiliations: [a]School of Environmental and Chemical Engineering, Jiangsu University of Science and Technology, Zhenjiang, Jiangsu 212100, China; [b]School of Chemistry and Chemical Engineering, Yangzhou University, Yangzhou 225002, China; [c]School of Material Science and Engineering, Jiangsu University of Science and Technology, Zhenjiang 212100, China; [d]State Key Laboratory of Materials-Oriented Chemical Engineering, College of Chemical Engineering, Nanjing Tech University, Nanjing 211816, China; [e]School of Chemistry and Chemical Engineering, Jiangsu University, Zhenjiang 212013, China; [f]Qingdao Institute of Bioenergy and Bioprocess Technology, Chinese Academy of Sciences, Qingdao 266101, China; [g]School of Environmental Science and Engineering, Nanjing Tech University, Nanjing 211816, China; and [h]Natural Sciences and Science Education, National Institute of Education, Nanyang Technological University, Singapore 637616, Singapore

1. V. Smil, Detonator of the population explosion. *Nature* **400**, 415–415 (1999).
2. R. F. Service, *New Recipe Produces Ammonia from Air, Water, and Sunlight* (American Association for the Advancement of Science, 2014).
3. P. Wei *et al.*, Electrocatalytic N_2 reduction to NH_3 with high Faradaic efficiency enabled by vanadium phosphide nanoparticle on V foil. *Nano Res.* **13**, 2967–2972 (2020).
4. J.-T. Ren, C.-Y. Wan, T.-Y. Pei, X.-W. Lv, Z.-Y. Yuan, Promotion of electrocatalytic nitrogen reduction reaction on N-doped porous carbon with secondary heteroatoms. *Appl. Catal. B: Environ.* **266**, 118633 (2020).
5. A. Liu *et al.*, A two-dimensional Ru@ MXene catalyst for highly selective ambient electrocatalytic nitrogen reduction. *Nanoscale* **12**, 10933–10938 (2020).
6. M. A. Mushtaq *et al.*, Photoelectrochemical reduction of N_2 to NH_3 under ambient conditions through hierarchical $MoSe_2$@gC_3N_4 heterojunctions. *J. Mater. Chem. A* **9**, 2742–2753 (2021).
7. M. Arif *et al.*, Highly active sites of NiVB nanoparticles dispersed onto graphene nanosheets towards efficient and pH-universal overall water splitting. *J. Energy Chem.* **58**, 237–246 (2021).
8. G. Yang *et al.*, Electrochemical fixation of nitrogen by promoting N_2 adsorption and N-N triple bond cleavage on the CoS_2/MoS_2 nanocomposite. *ACS Appl. Mater. Interfaces* **13**, 21474–21481 (2021).
9. M. Arif *et al.*, Hierarchical hollow nanotubes of NiFeV-layered double hydroxides@CoVP heterostructures towards efficient, pH-universal electrocatalytical nitrogen reduction reaction to ammonia. *Appl. Catal. B: Environ.* **265**, 118559 (2020).

10. R. Schlögl, Catalytic synthesis of ammonia–A "never-ending story"? *Angew. Chem. Int. Ed. Engl.* **42**, 2004–2008 (2003).
11. A. Hellman, K. Honkala, S. Dahl, C. Christensen, J. Nørskov, "Ammonia synthesis: State of the bellwether reaction" in *Comprehensive Inorganic Chemistry II (Second Edition): From Elements to Applications*, J. Reedijk, K. Poeppelmeier, Eds. (Elsevier Ltd., 2013), vol. 7, pp. 459–474.
12. C. Smith, A. K. Hill, L. Torrente-Murciano, Current and future role of Haber–Bosch ammonia in a carbon-free energy landscape. *Energy Environ. Sci.* **13**, 331–344 (2020).
13. L. Han *et al.*, Atomically dispersed molybdenum catalysts for efficient ambient nitrogen fixation. *Angew. Chem. Int. Ed. Engl.* **131**, 2343–2347 (2019).
14. C. Chen, Y. Liu, Y. Yao, Ammonia synthesis via electrochemical nitrogen reduction reaction on iron molybdate under ambient conditions. *Eur. J. Inorg. Chem.* **2020**, 3236–3241 (2020).
15. G. Qing *et al.*, Recent advances and challenges of electrocatalytic N_2 reduction to ammonia. *Chem. Rev.* **120**, 5437–5516 (2020).
16. T. Wu *et al.*, Greatly improving electrochemical N_2 reduction over TiO_2 nanoparticles by iron doping. *Angew. Chem. Int. Ed. Engl.* **58**, 18449–18453 (2019).
17. Y. Ren *et al.*, Strategies to suppress hydrogen evolution for highly selective electrocatalytic nitrogen reduction: Challenges and perspectives. *Energy Environ. Sci.* **14**, 1176–1193 (2021).
18. Y. Liu *et al.*, Electrocatalytic reduction of nitrogen on FeAg/Si for ammonia synthesis: A simple strategy for continuous regulation of faradaic efficiency by controlling H^+ ions transfer rate. *Appl. Catal. B: Environ.* **283**, 119606 (2021).
19. M. M. Shi *et al.*, Au sub-nanoclusters on TiO_2 toward highly efficient and selective electrocatalyst for N_2 conversion to NH_3 at ambient conditions. *Adv. Mater.* **29**, 1606550 (2017).
20. J. Fu, Y. Yang, J.-S. Hu, Dual-sites tandem catalysts for C–N bond formation via electrocatalytic coupling of CO_2 and nitrogenous small molecules. *ACS Mater. Lett.* **3**, 1468–1476 (2021).
21. L.-P. Yuan *et al.*, Phosphorus-doping activates carbon nanotubes for efficient electroreduction of nitrogen to ammonia. *Nano Res.* **13**, 1376–1382 (2020).
22. H. Jin *et al.*, Nitrogen vacancies on 2D layered W_2N_3: A stable and efficient active site for nitrogen reduction reaction. *Adv. Mater.* **31**, 1902709 (2019).
23. R. Jing *et al.*, Cas9-cleavage sequences in size-reduced plasmids enhance nonviral genome targeting of CARs in primary human T cells. *Small Methods* **5**, 2100071 (2021).
24. S. B. Patil, D. Y. Wang, Exploration and investigation of periodic elements for electrocatalytic nitrogen reduction. *Small* **16**, 2002885 (2020).
25. L. Yang *et al.*, Flower-like hollow $MoSe_2$ nanospheres as efficient earth-abundant electrocatalysts for nitrogen reduction reaction under ambient conditions. *Inorg. Chem.* **59**, 12941–12946 (2020).
26. W. Ye *et al.*, Fe, Mo-N/C hollow porous nitrogen-doped carbon nanorods as an effective electrocatalyst for N_2 reduction reaction. *ACS Sustain. Chem. Eng.* **8**, 15946–15952 (2020).
27. Y. Luo *et al.*, Efficient electrocatalytic N_2 fixation with MXene under ambient conditions. *Joule* **3**, 279–289 (2019).
28. H. Zhao *et al.*, High-performance nitrogen electroreduction at low overpotential by introducing Pb to Pd nanosponges. *Appl. Catal. B: Environ.* **265**, 118481 (2020).
29. F. Pang *et al.*, Bimodal nanoporous Pd3Cu1 alloy with restrained hydrogen evolution for stable and high yield electrochemical nitrogen reduction. *Nano Energy* **58**, 834–841 (2019).
30. J. Chen *et al.*, Redispersion of Mo-based catalysts and the rational design of super small-sized metallic Mo species. *ACS Catal.* **9**, 5302–5307 (2019).
31. H. Wang *et al.*, Electrochemical fabrication of porous Au film on Ni foam for nitrogen reduction to ammonia. *Small* **15**, 1804769 (2019).
32. L. Zhang *et al.*, A janus Fe-SnO_2 catalyst that enables bifunctional electrochemical nitrogen fixation. *Angew. Chem. Int. Ed. Engl.* **132**, 10980–10985 (2020).
33. Y. T. Liu, X. Chen, J. Yu, B. Ding, Carbon-nanoplated CoS@TiO_2 nanofibrous membrane: An interface-engineered heterojunction for high-efficiency electrocatalytic nitrogen reduction. *Angew. Chem. Int. Ed. Engl.* **58**, 18903–18907 (2019).
34. B. Qin *et al.*, Understanding of nitrogen fixation electro catalyzed by molybdenum–iron carbide through the experiment and theory. *Nano Energy* **68**, 104374 (2020).
35. W. Qiu *et al.*, High-performance artificial nitrogen fixation at ambient conditions using a metal-free electrocatalyst. *Nat. Commun.* **9**, 3485 (2018).
36. M. Peng *et al.*, Bioinspired Fe_3C@C as highly efficient electrocatalyst for nitrogen reduction reaction under ambient conditions. *ACS Appl. Mater. Interfaces* **11**, 40062–40068 (2019).
37. X. Ren *et al.*, Electrochemical N_2 fixation to NH_3 under ambient conditions: Mo_2N nanorod as a highly efficient and selective catalyst. *Chem. Commun.* **54**, 8474–8477 (2018).
38. X. Yang *et al.*, Mechanistic insights into electrochemical nitrogen reduction reaction on vanadium nitride nanoparticles. *J. Am. Chem. Soc.* **140**, 13387–13391 (2018).
39. Y. Yang *et al.*, The crucial role of charge accumulation and spin polarization in activating carbon-based catalysts for electrocatalytic nitrogen reduction. *Angew. Chem. Int. Ed. Engl.* **59**, 4525–4531 (2020).
40. Y. Liu *et al.*, Facile ammonia synthesis from electrocatalytic N_2 reduction under ambient conditions on N-doped porous carbon. *ACS Catal.* **8**, 1186–1191 (2018).
41. X. Wang, M. Luo, J. Lan, M. Peng, Y. Tan, Nanoporous intermetallic Pd_3Bi for efficient electrochemical nitrogen reduction. *Adv. Mater.* **33**, 2007733 (2021).
42. Y. Zhang *et al.*, Electrochemical synthesis of ammonia from nitrogen catalyzed by $CoMoO_4$ nanorods under ambient conditions. *J. Mater. Chem. A* **9**, 5060–5066 (2021).
43. Y. Wan, Z. Wang, J. Li, R. Lv, Mo_2C-MoO_2 heterostructure quantum dots for enhanced electrocatalytic nitrogen reduction to ammonia. *ACS Nano* **16**, 643–654 (2021).
44. H. Fei *et al.*, Sulfur vacancy engineering of MoS_2 via phosphorus incorporation for improved electrocatalytic N_2 reduction to NH_3. *Appl. Catal. B: Environ.* **300**, 120733 (2022).
45. J. Han *et al.*, MoO_3 nanosheets for efficient electrocatalytic N_2 fixation to NH_3. *J. Mater. Chem. A* **6**, 12974–12977 (2018).
46. F. Shaqi *et al.*, Defect and interface engineering of hexagonal Fe_2O_3/$ZnCo_2O_4$ nn heterojunction for efficient oxygen evolution reaction. *Appl. Catal. B: Environ.* **333**, 122813 (2023).